



Enhanced photocatalytic H₂ production independent of exciton dissociation in crystalline carbon nitride

Guoqiang Zhang^a, Yangsen Xu^c, Jinyu Zhu^b, Yongliang Li^b, Chuanxin He^b, Xiangzhong Ren^b, Peixin Zhang^b, Hongwei Mi^{b,*}

^a School of Physical Sciences, Great Bay University, Dongguan, Guangdong 523808, PR China

^b College of Chemistry and Environmental Engineering, Shenzhen University, Shenzhen, Guangdong 518060, PR China

^c Institute of Information Technology, Shenzhen Institute of Information Technology, Shenzhen, Guangdong 518172, PR China

ARTICLE INFO

Keywords:

Crystalline carbon nitride
In-plane crystallinity
Exciton dissociation
Carrier mobility
Charge separation

ABSTRACT

The role of exciton dissociation in charge separation dominated by in-plane crystallinity has been rarely addressed, although it is the decisive step of polymeric carbon nitride (CN) photocatalysis. Here, taking ten kinds of crystalline carbon nitride (CCN) as examples, the relationship between exciton dissociation, carrier mobility, conductivity, charge separation and photocatalytic activity under different in-plane crystallinity has been investigated. Although the in-plane crystallinity dominates charge separation and photocatalytic activity, it does not significantly reduce excitons binding energy (EBE) or improve exciton dissociation efficiency (EDE), only decreasing by 1.5 meV and increasing by 2.3 %, respectively. It is the greatly improved carrier mobility and conductivity that are more responsible for the increased charge separation and photocatalytic activity than the slight change in EDE. To our knowledge, this is the first reported case of overall water splitting in CCN of poly (heptazine imide) structure, resulting from the optimized in-plane crystallinity.

1. Introduction

Different from inorganic semiconductors with strong screening effects and large dielectric properties, polymeric carbon nitride (CN), as the most typical polymer photocatalysts, exhibits strong intrinsic Coulomb interactions of electron-hole pairs, that is, far greater than excitons binding energy (EBE) of inorganic photocatalysts [1–3]. Such large EBE makes photogenerated carriers mainly exist in the form of singlet Frenkel excitons. However, Frankel excitons need to overcome the strong Coulomb interactions to become free electrons and holes. Subsequently, free carriers undergo diffusion motion or drift motion to produce spatial separation before participating in photocatalytic reactions [4–6]. As a result, the large EBE greatly limits excitons dissociation, resulting in unsatisfactory charge separation and photocatalytic efficiency of CN-based materials [7]. Theoretically, their charge separation and photocatalytic activity is likely to be dependent on exciton dissociation behavior [8–10].

Optimization of crystallinity is an important strategy to improve the charge separation and photocatalytic activity of CN-based materials. Wang's group successfully prepared in-plane highly ordered crystalline

carbon nitride (CCN) nanosheets, exhibiting excellent photocatalytic performance [11]. Zhao et al. demonstrated that in-plane integrity conduces more to accelerating charge separation and photocatalytic activity than interlayer stacking order [12]. Our previous work elucidated that the in-plane crystallinity dominates charge separation and photocatalytic activity in CCN [13]. Given that charge separation and photocatalytic activity is highly dependent on exciton dissociation, it is rational to speculate whether the enhanced photocatalytic activity is determined by the facilitated exciton dissociation behavior. In addition, the optimization of in-plane crystallinity will accelerate the rapid in-plane transport of carriers, thus improving the carrier mobility and conductivity [13–15]. The highly-crystalline BaZrO₃ has fewer grain boundaries and can act as a "highway" for carrier transport, resulting in better charge separation and photocatalytic performance [16]. Or is it the improved in-plane crystallinity that leads to the increased carrier mobility and conductivity, rather than the enhancement of exciton dissociation, thus promoting the charge separation and photocatalytic activity? However, few studies have been conducted, although it is an important decisive step in the charge separation of layered photocatalysts and photoelectric conversion materials.

* Corresponding author.

E-mail address: milia807@szu.edu.cn (H. Mi).

<https://doi.org/10.1016/j.apcatb.2023.123049>

Received 12 April 2023; Received in revised form 12 June 2023; Accepted 24 June 2023

Available online 11 July 2023

0926-3373/© 2023 Elsevier B.V. All rights reserved.

Here, ten kinds of CCN with poly(heptazine imide) (PHI) structure were taken as examples to investigate the exciton dissociation behavior, carrier mobility and photocatalytic activity under different in-plane crystallinity. The obtained results show that the elevated in-plane crystallinity does not significantly promote exciton dissociation. On the contrary, the optimization of in-plane crystallinity greatly improves the carrier mobility and conductivity of CCN, thus accelerating charge separation and photocatalytic activity for H_2 production. However, it should be emphasized that the role of exciton dissociation in photocatalysis has not been denied here, but the enhanced in-plane crystallinity does not significantly promote exciton dissociation.

2. Experimental section

2.1. Chemicals and materials

Melamine (99 %), NaCl (AR, 99.5 %), KCl (AR, 99.5 %) and LiCl (AR, 99.0 %) were purchased from Macklin Reagent Company. $H_2PtCl_6 \cdot 6H_2O$ (AR, Pt \geq 37.5 %) and triethanolamine (TEOA, AR, 98.0 %) were purchased from Aladdin Reagent Company.

2.2. Preparation of CN (melon)

The 50 g of melamine powder was placed into a 200 mL of crucible with a cover (sealed with tin foil) and then heat to 550 °C at a rate of 2 °C/min for 3 h (in the air). The 28.7 g of CN (yield: 57.4 %) was obtained after cooled to room temperature.

2.3. Preparation of CCN by NaCl-LiCl molten-salt with different proportions

The 1.5 g of CN powder, 3.5–8 g of NaCl and 6.5–2 g of LiCl (keeping the weight of the mixed salts at 10 g) were added to a 20 mL of crucible with a cover (sealed with tin foil) and then heat to 600 °C at a rate of 2 °C/min for 4 h (in the air). Note: placing the mixed salt above CN is beneficial to completely cover CN and isolate air when molten salt melts. The products were obtained after cooled to room temperature, washed three times with water and dried at 60 °C under vacuum. According to different NaCl-LiCl molten-salt proportions, the final samples (1.50–1.55 g) were named Na/Li 3.5/6.5, Na/Li 5/5, Na/Li 6.5/3.5 and Na/Li 8/2, respectively.

2.4. Preparation of CCN by NaCl-LiCl (5/5) molten-salt under different holding times (2–12 h)

The synthesis conditions of the samples were consistent with those in 2.3, except that the proportion of molten-salt was maintained at 5/5 and the holding times were regulated for 2–12 h. According to different holding times, the final samples (1.50–1.55 g) were named CCN-2, CCN-4 (Na/Li 5/5), CCN-6, CCN-8 and CCN-12, respectively.

2.5. Preparation of CCN-Na by NaCl solid-salt

The synthesis conditions were the same as CCN-6, except for grinding and mixing CN and NaCl solid-salt. Finally, the 1.41 g of CCN-Na sample was obtained.

2.6. Preparation of CCN-K/Li by KCl-LiCl molten-salt

The synthesis conditions were the same as CCN-6 except for the use of KCl-LiCl (5/5) molten-salt. Finally, the 1.52 g of CCN-K/Li sample was obtained.

3. Results and discussion

3.1. Preparation process and morphology characterization

The preparation process of CCN is shown in Fig. 1. Traditional CN thermal polymerization process always faces the problem of incomplete polymerization, resulting in the formation of amorphous melon ($C_{12}N_{18}H_6$) structure, in which there are abundant unpolymerized amino groups and hydrogen bonds between melon chains [17,18]. With the NaCl-LiCl molten-salt acting as the solvent to promote mass transfer, the unpolymerized amino groups will further polymerize to form crystalline PHI ($C_{12}N_{17}H_3$) structure [19]. Thus, the further polymerization of the unpolymerized amino group leads to the enhancement of in-plane crystallinity. Additionally, the widely-used solid-salts of KCl [13,20–22] or NaCl [11], or the low-melting-point of KCl-LiCl molten-salt [23–25] (~350 °C) were not selected here. The high-melting-point of NaCl-LiCl molten-salt (~550 °C) was adopted because of the higher in-plane crystallinity and photocatalytic efficiency of CCN prepared in NaCl-LiCl than other molten-salts and solid-salts. In addition, unlike previous reports that require mixing molten-salt in a glove box and heat treatment for crystallization in an inert atmosphere [23–25], our entire operation was completed in the air. This may be because the molten-salt placed above the CN can completely cover the CN and isolate the air during melting [3]. The in-plane crystallinity of CCN was regulated by adjusting different proportions (3.5/6.5–8/2) of NaCl-LiCl molten-salt and holding times (2–12 h) at 600 °C.

The representative morphologies of the samples were characterized by field emission scanning electron microscope (FE-SEM) and transmission electron microscopy (TEM). As shown in Fig. 2a-d and g, CN presents a typical micron-scale bulk amorphous structure, while CCN exhibits nanorod arrays with a thickness of 50–100 nm. The BET specific surface areas and pore size distributions were measured by nitrogen isothermal adsorption-desorption. All samples show II-type isothermal adsorption curves with H3-type hysteresis loops (Fig. 2e), indicating the existence of macroporous structures stacked by amorphous structures or nanorods. The specific surface areas were measured as 9.9, 96.4, 113.2 and 128.0 m²/g for CN, CCN-2, CCN-6 and CCN-12, respectively. The pore size distribution curves further confirm the macroporous structures with about tens of nanometers (Fig. 2f).

The clear lattice fringes with a spacing of 1.12 nm along the nanorods direction are observed in high-resolution TEM (HR-TEM) images (inset in Fig. 2h), which corresponds to the (100) crystal plane [11,26]. Besides, the diffraction points of (100), (110), (002) and (320) crystal planes are detected from the selected area electron diffraction (SAED, Fig. 2i) pattern [26]. These results indicate the highly-crystalline single-crystal of nanorods of CCN-6, facilitating charge transport along the nanorods direction. Moreover, scanning TEM (STEM) with energy dispersive X-ray is performed to analyze the elements distribution in CCN-6 sample. The C, N and Na elements are uniformly distributed in the selected nanorod region (Fig. 2k-m). Trace amounts of Cl element could be derived from the surface absorption of Cl⁻ ion (Fig. 2n) [4], while Li is a light element and cannot be detected in elemental mappings.

3.2. Structural characterization

Theoretically, the in-plane charge transport barrier is much smaller than that between interlayer in layered CN-based materials. Kang et al. calculated that the in-plane electrostatic potentials are much lower than the interlayer, indicating that the in-plane charge transport is far more favorable than the interlayer [27]. Our previous work elucidated that the in-plane crystallinity dominates charge separation and photocatalytic activity in heptazine-based K⁺ ion implanted CCN [13], inspiring us to further regulate the in-plane crystallinity of Na-PHI. The CN (melon) was further polymerized and crystallized under different proportions (3.5/6.5–8/2) of NaCl-LiCl molten-salts and different

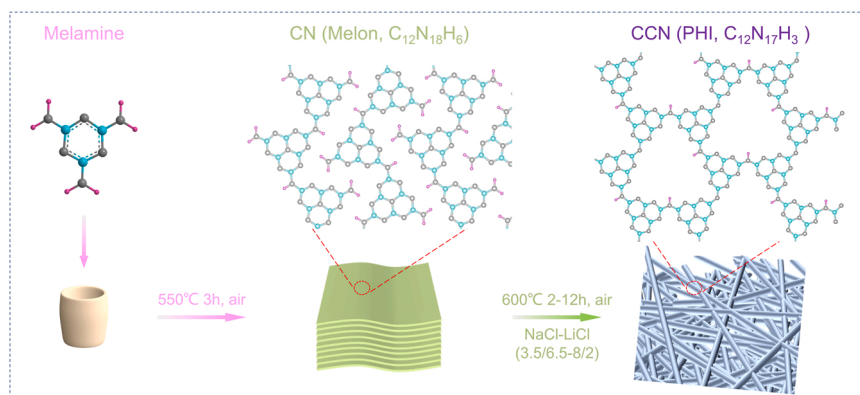


Fig. 1. Preparation process of CCN. The atoms of C, N and H are in white, gray and purple, respectively.

holding times (2–12 h) at 600 °C, which successfully realized the regulation of in-plane crystallinity of Na-PHI. The X-ray diffraction (XRD) patterns of corresponding samples are shown in Fig. 3a,b. Two typical diffraction peaks of CN at 13.0 and 27.7° correspond to the (100) and (002) crystal planes, while CCN exhibits two new peaks attributed to the in-plane periodic (100) and (110) planes at 8.0 and 14.3°, respectively [26].

The interlayer (002) diffraction peaks at 26.5 and 27.8° can be attributed to different stacking patterns between the layers with a spacing of 0.336 and 0.321 nm, respectively [28]. As can be observed from Fig. 3a, the CCN structure implanted with Na⁺ ion is prone to form interlayer stacking with a spacing of 0.321 nm, while the intercalation of Li⁺ ion is more inclined to 0.336 nm stacking. Among the samples under four molten-salts, Na/Li 5/5 presents the highest in-plane crystallinity, so the optimized proportion of NaCl-LiCl molten-salt was 5/5. Then the effect of holding times on the in-plane crystallinity was investigated under the optimized NaCl-LiCl molten-salt (5/5) (Fig. 3b). With the extension of holding times from 2 to 12 h, the in-plane crystallinity first increases and then decreases. CCN-6 shows the highest in-plane crystallinity in all samples, far more than CCN-Na and CCN-K/Li constructed with NaCl solid-salt and KCl-LiCl molten-salt, respectively.

The inductively coupled plasma optical emission spectrometer (ICP-OES, Table S1) measurements reveal that the Li and Na element contents in CCN-*x* (*x* = 2, 6, 12) samples are approximately 1.78–1.66 wt % and 3.84–3.71 wt %, respectively. In the CCN-Li/K sample, the Li and K element contents are 1.52 wt % and 5.86 wt % (Table S2). The previously reported PHI synthesized with KCl-LiCl molten-salt at 550 °C basically contains no Li element [23–25]. These PHI constructed here all contain some Li element, probably because the higher temperature (600 °C) makes Li participate in the formation of PHI structure.

Elemental analysis (Table S3) demonstrates that the C/N molar ratio in CN was 0.656, which is close to 0.667 in melon (C₁₂N₁₈H₆). As CN was further polymerized and crystallized in NaCl-LiCl and KCl-LiCl molten-salts or NaCl solid-salt, the C/N ratio of all CCN samples approaches 0.706 of PHI (C₁₂N₁₇H₃). Based on the C/N ratio of CCN and ideal melon (0.667) and PHI (0.706), the proportion of unpolymerized amino group can be calculated to be 12.5 %, 4.8 %, 0 %, 2.3 % and 7.4 % for CCN-2, CCN-4, CCN-6, CCN-8 and CCN-12, respectively. Although the C/N ratio only increases by 0.005 (CCN-2 vs. CCN-6), the unpolymerized amino group decreases by 12.5 %. Interestingly, the stronger the in-plane crystallinity of CCN, the closer the C/N molar ratio is to 0.706, which indicates that the accelerated polymerization of free amino groups leads to highly-crystalline PHI. Thermogravimetric analysis (Fig. S1) indicates that CN has no obvious weight loss below 600 °C, while CCN-6 presents a typical water loss signal (14.6 wt % water) between 50 and 200 °C. According to previous reports [19], the PHI has better water absorption compared to CN, capable of absorbing 10–20 wt % water, and the water inside the pores has a major influence on the 3D stacking structure.

Therefore, CCN-6 presents a typical water loss signal. Both CN and CCN-6 decompose violently after 600 °C and completely at 800 °C. Due to the presence of Li and Na elements, CCN-6 remains 25.4 % at 800 °C, while CN is completely absent.

Fourier transform infrared spectroscopy (FTIR, Fig. 3c) is performed to investigate the representative structures of the samples. The signal at 814 cm⁻¹ belongs to the out-of-plane bending of the heptazine-ring. The pattern at 993 cm⁻¹ is assigned to the symmetric and asymmetric vibration of the NC₂ bond in metal-NC₂ unit [23,29], indicating the presence of Na/Li-NC₂ groups. Besides, the peaks at 1200–1700 cm⁻¹ represent the stretching and bending vibration of conjugated heterocycles in heptazine structures [30], and the signal at 2182 cm⁻¹ belongs to the asymmetric stretching mode of cyanogroup [31]. The possible structures and skeletons are further analyzed by solid-state CP/MAS ¹³C nuclear magnetic resonance (NMR, Fig. 3d). A new NMR peak at 168.3 ppm originates from CN₂(N⁻) structure [21], while the two signals at 156.8 and 165.4/163.5 ppm can be attributed to carbon atoms in C-N₃ and CN₂-(NH_x) units, affirming the heptazine-based skeletons in CN and CCN [32].

UV-vis diffuse reflectance spectroscopy (UV-vis DRS, Fig. 3e) indicates that the absorption band edge redshifted from 454.5 to 466.7 nm after further polymerization and crystallization of CN to form CCN, consistent with the deepened yellow appearance of the samples (inset in Fig. 3e). The calculated bandgap is reduced from 2.80 eV (CN) to 2.74 eV (CCN) according to the Tauc plots (inset in Fig. 3e). The steeper absorption edge and narrower bandgap is attributed to the improved conjugated structure due to higher polymerization degree and crystallinity. The valence band X-ray photoelectron spectroscopy (VB-XPS, Fig. 3f) demonstrates that the valence band positions of CN and CCN-6 remain unchanged and are 1.98 eV below the Fermi level. As shown in the band position diagram (inset in Fig. 3f), the narrowed bandgap of CCN-6 is mainly caused by the reduction of conduction band position by 0.06 eV.

The possible chemical structure changes were investigated by XPS measurement. The survey XPS spectra (Fig. 4a) reveal the presence of C, N and O elements in both CN and CCN-6, while Na element only exists in CCN-6. The high-resolution XPS spectra of Li 1s (Fig. 4b) at 54.8 eV and Na 1s (Fig. 4c) at 1071.2 eV in CCN-6 demonstrate the main existence of Li⁺ and Na⁺ ions in PHI structure [26,33]. The XPS peak of Cl 2p is at 199.2 and 197.1 eV (Fig. 4d), which is close to the Cl⁻ ions in KCl [34]. This is also consistent with previous reports that trace amounts of Cl⁻ ions remain in CCN [4,13]. Therefore, we speculate that the residual Cl in the sample may come from the Cl⁻ ions adsorbed on the surface (less than 0.2 wt %). In C 1s XPS spectrum (Fig. 4e), two Gaussian peaks at 288.1 and 284.7 eV are identified as the C atoms in the aromatic N-C=N and C-C units [35,36]. And the middle peak at 286.3 eV is assigned as the C≡N species [37]. The N 1s XPS spectrum (Fig. 4f) can be fitted into three components at 398.7, 400.3 and 401.3 eV, respectively, corresponding to the N atoms of C-N=C, N-(C)₃ and bridged NH_x in heptazine

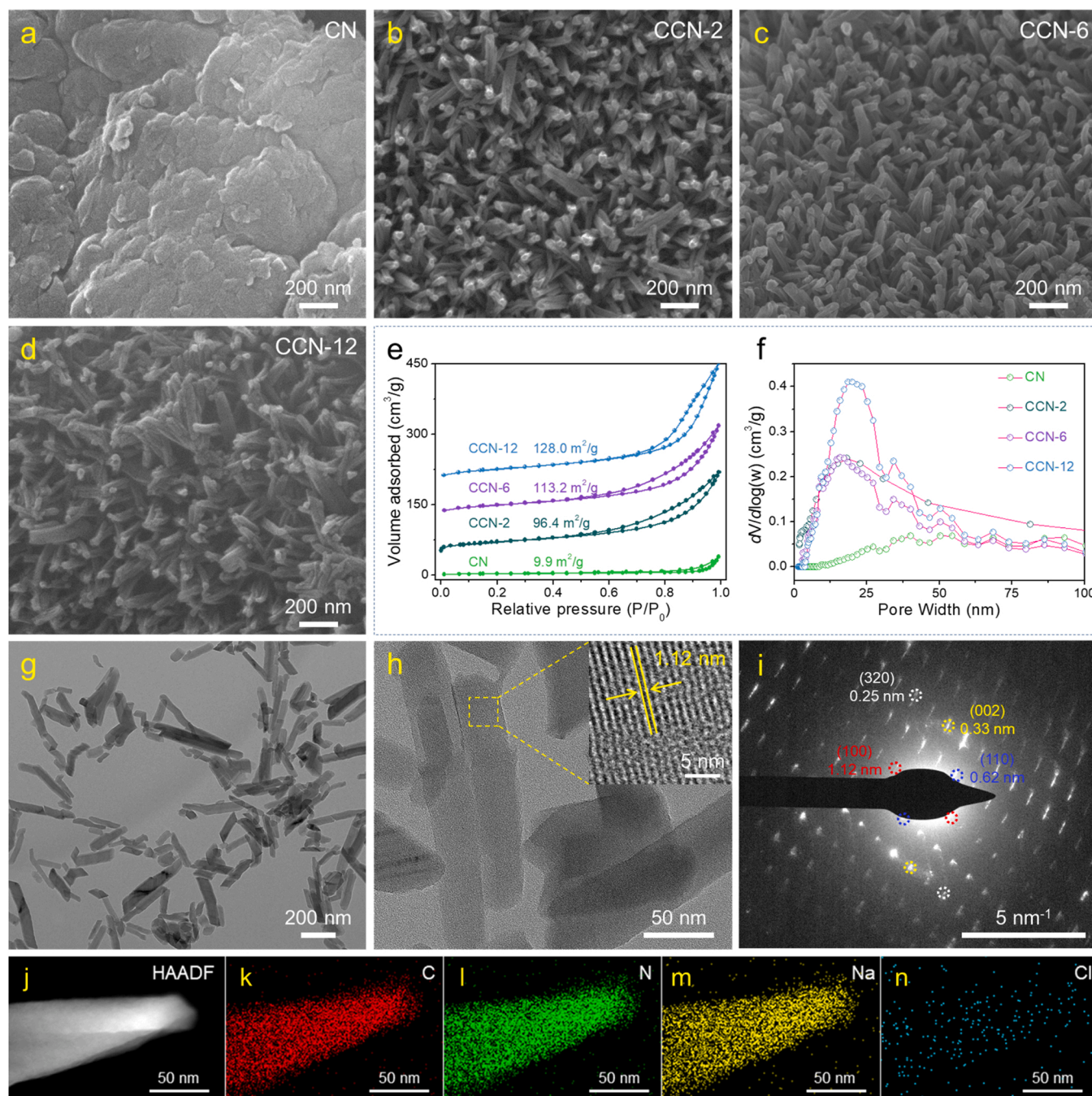


Fig. 2. SEM images (a-d), the N₂ adsorption-desorption isotherms (e) and pore size distribution curves (f) of CN and CCN-*x* (*x* = 2, 6, 12). TEM images (g-h) of CCN-6. Inset in (h) is the HR-TEM image. The SAED pattern (i), STEM image (j) and the corresponding elemental mappings (k-n) of CCN-6.

unit [35,38]. Overall, these characterizations, involving TEM, XRD, elemental analysis, FTIR NMR, UV-Vis DRS and XPS, confirm the highly polymerized and crystallized heptazine-based PHI structure of CCN with extended light absorption, compared to CN. More importantly, the in-plane crystallinity of a series of CCN has been optimized by adjusting the type of molten-salts (NaCl-LiCl and KCl-LiCl) or solid-salt (NaCl), different proportions of NaCl-LiCl molten-salts (3.5/6.5–8/2) and different holding times (2–12 h).

3.3. Measurement of photocatalytic activity

The optimized in-plane crystallinity of CCN is expected to have excellent photocatalytic activity. The visible-light driven H₂ production

activity was measured with TEOA (10 vol %) as sacrificial agent and Pt (3 wt %) as co-catalyst, and the test temperature was controlled at 5 °C by recirculating cooling water system. It should be noted that CN and CCN samples alone, even in the presence of TEOA sacrificial agents, cannot produce H₂ due to the lack of hydrogen-producing active sites. As shown in Fig. 5a, among CCN constructed with different NaCl-LiCl molten-salt proportions, Na/Li 5/5 (CCN-4) presents the highest activity of 203.1 μmol/h. Then the influence of holding times on the activity was explored under the optimized NaCl-LiCl molten-salt (5/5) (Fig. 5b). With the prolongation of holding times (2–12 h), the activity increases first and then decreases. CCN-6 exhibits the highest visible-light H₂ production rate of 304.0 μmol/h in all samples, which is 59.6 times that of CN (5.1 μmol/h), and 11.7 and 4.9 times that of CCN-Na (25.9 μmol/

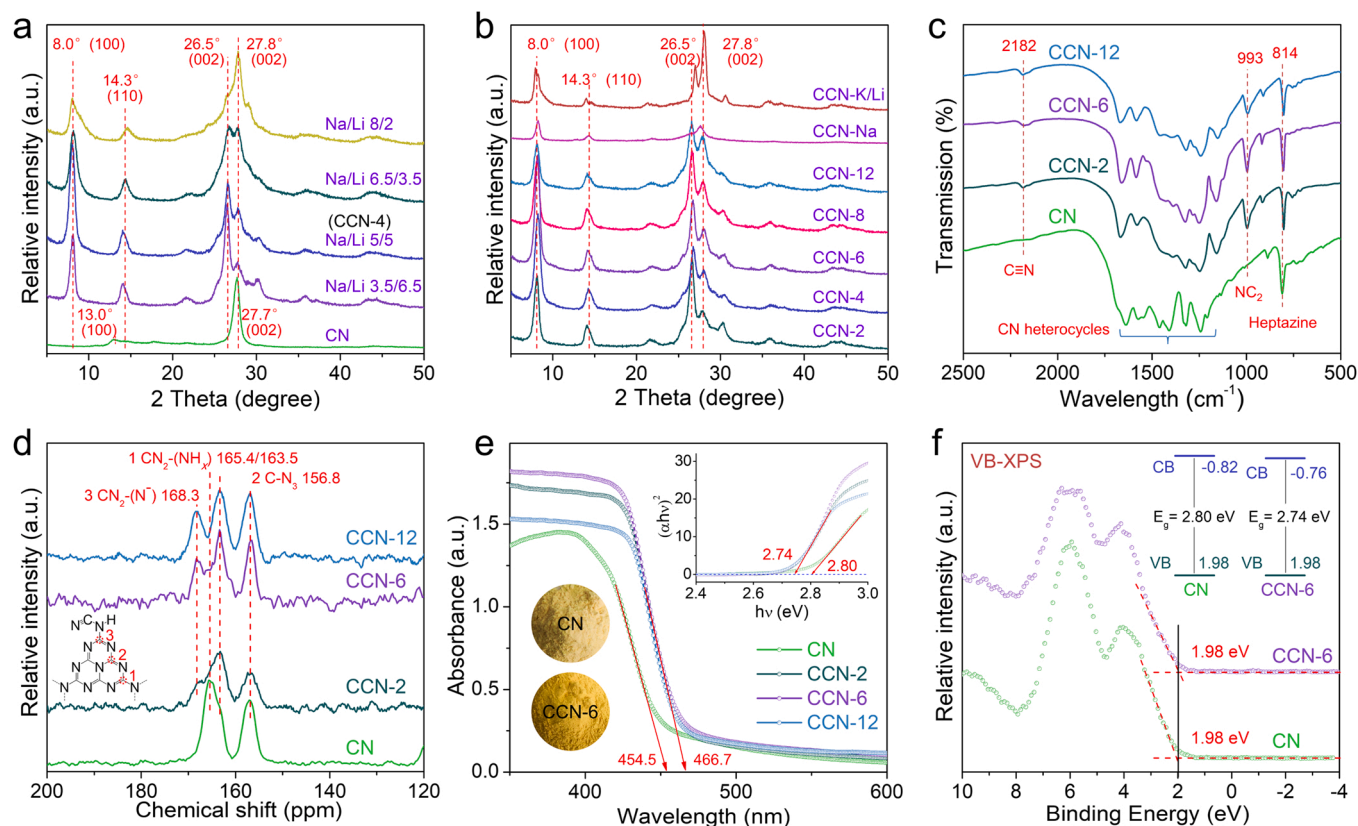


Fig. 3. XRD patterns (a-b), FTIR spectra (c), solid-state CP/MAS ^{13}C NMR spectra (d) and UV-Vis DRS spectra (e). Insets in (e) are the optical photos and Tauc plots. VB-XPS (f) and band position diagram (inset).

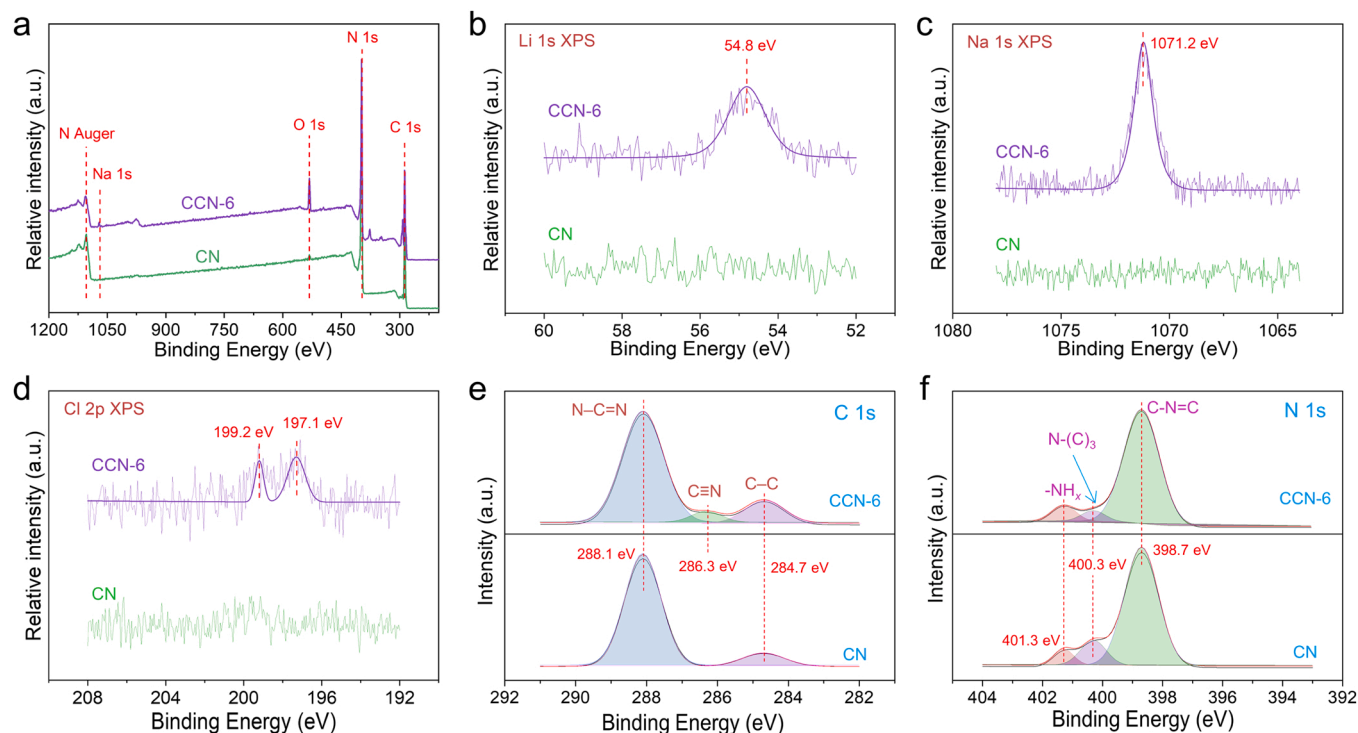


Fig. 4. The survey XPS spectra (a) and high-resolution XPS spectra (b-f) of CN and CCN-6.

h) and CCN-K/Li (62.1 $\mu\text{mol/h}$) constructed with NaCl solid-salt and KCl-LiCl molten-salt. These changes in photocatalytic performance are probably caused by the differences in the in-plane crystallinity, which

dominates the overall charge separation and photocatalytic activity [13].

The apparent quantum efficiency (AQE) is calculated by measuring

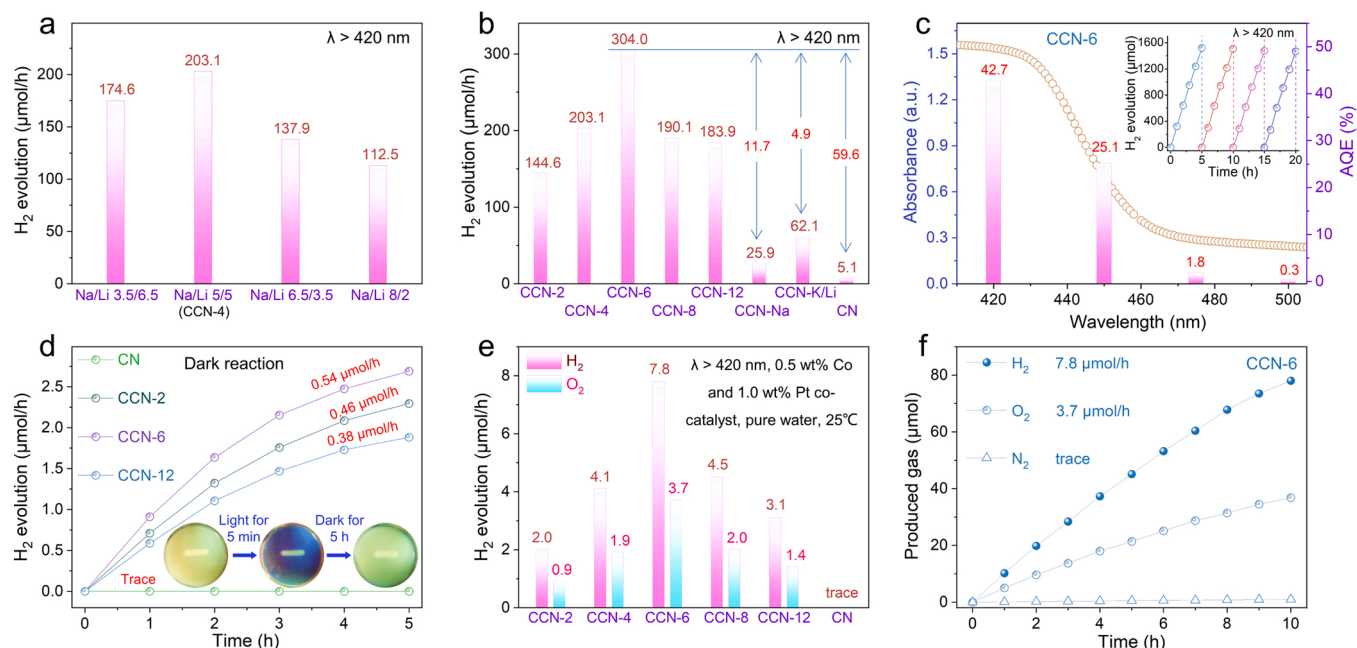


Fig. 5. H₂ production rates under visible-light irradiation (a–b). Wavelength-dependent AQE under monochromatic light irradiations (c) and the recycling measurements of H₂ production (inset). H₂ production in the dark (d) and overall water splitting under visible-light irradiation loaded with Co and Pt co-catalysts (e–f).

the H₂ production rate under different monochromatic light irradiations. The AQE of CCN-6 is consistent with the absorption change, showing 42.7 %, 25.1 % and 1.8 % at 420, 450 and 475 nm, respectively (Fig. 5c). And at 500 nm, its AQE is still 0.3 %. Such AQE at 420 nm is obviously higher than 10.9 % of OKCN [39], 17.8 % of BMCN [3], 23.5 % of TKCN [40], 25.7 % of KCCN [4], 26.1 % of K-CN [13] and 31.2 % of CKCN [20] in our previous work, probably due to the better in-plane crystallinity of CCN-6. In addition, the cyclic H₂ production test is conducted to characterize the photostability of the sample. As shown in the inset in Fig. 5c, after four cycles, that is, 20 h of continuous visible-light irradiation, the activity of CCN-6 only attenuates by 3.6 %. In addition, the visible-light photocurrent exhibits a slight attenuation after 400 s of irradiation (Fig. S2), further indicating relatively excellent photostability of CCN-6. In the presence of TEOA sacrificial agent and Pt co-catalyst, CCN-6 will form a photoreduction state with a very long life under visible-light irradiation [19,41,42]. As revealed in the inset in Fig. 5d, the yellow CCN-6 solution, which turns dark-blue when exposed to light, is attributed to the accumulation of electrons in the sample. The accumulated electrons then gradually release in the dark, reducing protons to produce H₂, and the corresponding color returns to yellow. The H₂ production in the dark after electron accumulation is shown in Fig. 5d. There is no color change in CN under illumination and H₂ is not detected in the dark, while the average dark H₂ production rates of CCN-2, CCN-6 and CCN-12 within five hours are 0.38, 0.54 and 0.46 μmol/h, respectively.

High in-plane crystallinity and low structural defects promote carrier transport and reduce recombination at defect sites, resulting in high photocatalytic performance. Such highly-crystalline ideal CCN provides the attempt to overall water splitting, the Holy Grail reaction in photocatalysis [43]. Choosing the appropriate co-catalyst is very important to break the kinetic limitations during the overall water splitting. According to the report by Wang et al. [44,45] Pt and Co (CoO_x) are very suitable for poly(triazine imide) to achieve overall water splitting, and electrons and holes are easily separated on the co-catalysts. Therefore, the Pt and Co co-catalysts were chosen to be loaded on CCN for H₂ and O₂ production. In order to further accelerate the rate of water splitting, the experimental temperature of 25 °C was adopted. As shown in Fig. 5e, stoichiometric ratios of H₂ and O₂ (H₂/O₂ ≈ 2/1) are simultaneously generated, indicating the overall water splitting in a series of CCN with

different in-plane crystallinity. In addition, the rate of water splitting is also consistent with the change of in-plane crystallinity. CCN-6 presents the highest in-plane crystallinity and overall water splitting activity (H₂: 7.8 μmol/h, O₂: 3.7 μmol/h) among all CCN. It can be seen from Fig. 5f that, unlike the instability of nitrides during overall water splitting, CCN produces stoichiometric ratios of H₂ and O₂ while no N₂ is detected, indicating relatively good photostability. It's worth noting that loading Pt or Co co-catalysts alone on CCN, or simultaneously loading Pt and Co co-catalysts on CN, cannot achieve overall water splitting. Thus, co-catalyst loading and optimization of crystallinity are both important for achieving overall water splitting, and may be even more important for the crystallinity of CN-based materials. To the best of our knowledge, this is the first reported case of overall water splitting in the CCN with PHI structure, which originates from the optimized in-plane crystallinity.

TEM, elemental mappings and XPS characterizations were supplemented to investigate the load of Pt and Co co-catalysts. Fig. S3 is the TEM image of CCN-6 loaded with Pt and Co co-catalysts. The lattice fringes of Pt were determined to be 0.23 nm. For Co species, no lattice fringes were observed, probably due to the amorphous structure or low crystallinity [45]. In addition, elemental mappings indicate that both Pt and Co elements were present on the surface of CCN-6 (Fig. S4). Fig. S5a shows the high-resolution XPS of Pt 4f, which can be attributed to Pt⁰ and Pt²⁺ [45]. The Co 2p XPS, as shown in Fig. S5b, confirms the formation of CoO_x species [45]. These characterizations all confirm the successful loading of Pt and Co co-catalysts.

3.4. Characterization of exciton dissociation, conductivity and carrier mobility

Unlike the low EBE of most inorganic photocatalysts, polymer photocatalysts, including CN and CCN, have considerable EBE that prevents exciton dissociation into free electrons and holes [7]. The bottleneck of exciton dissociation is expected to be one of the main factors restricting the photocatalytic activity in polymer photocatalysts [7]. The temperature-dependent photoluminescence (TD-PL) is an effective characterization of exciton dissociation behavior. As shown in the insets in Fig. 6a–f, the increased temperature from 25 to 300 K provides a driving force for the dissociation of excitons, and more dissociated

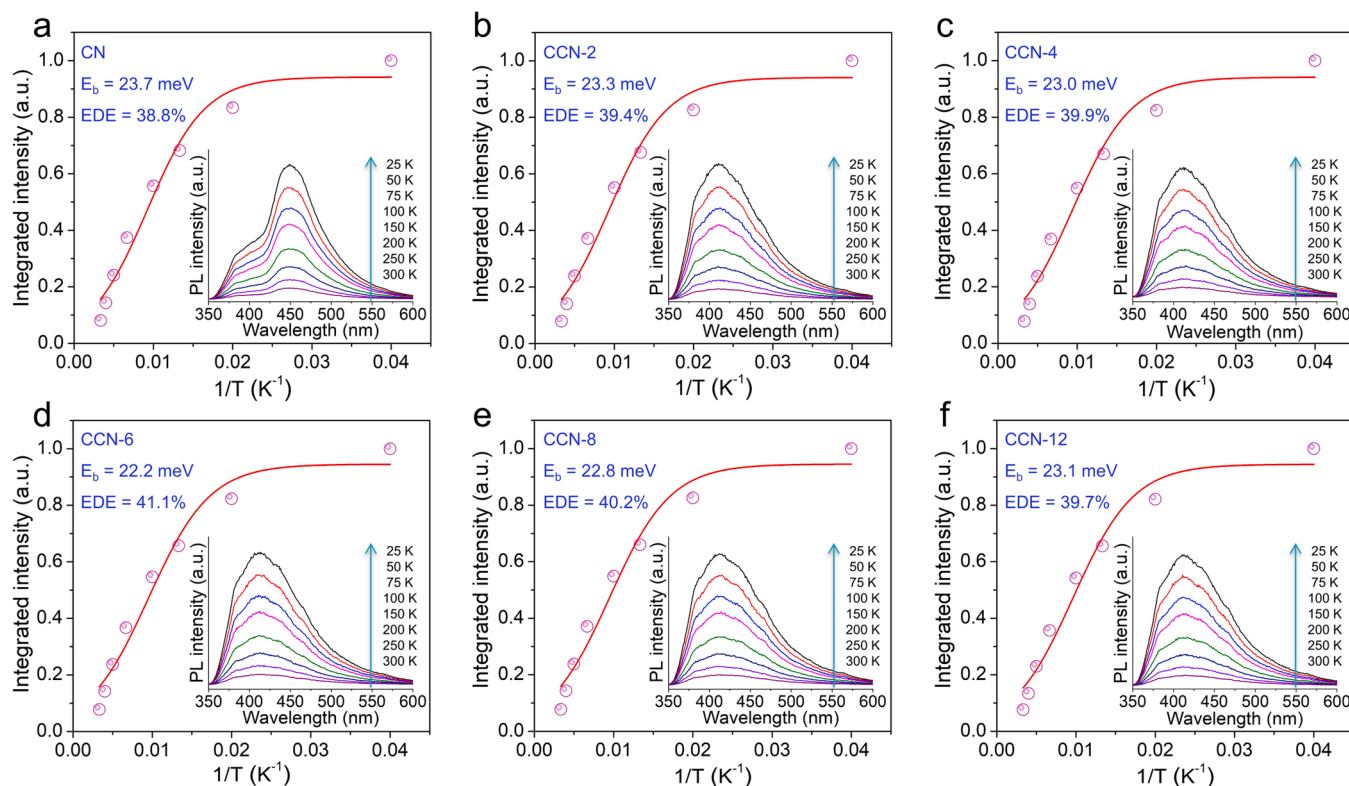


Fig. 6. TD-PL spectra (insets in a-f) from 25 to 300 K under 325 nm laser excitation. Integrated PL emission intensity as a function of temperature from 25 to 300 K (a-f).

excitons reduce the PL strength. Therefore, the functions of PL intensity and temperature can be fitted based on the equation " $I(T) = I_0 / (1 + Ae^{-E_b/(k_B T)})$ ", where I_0 is the PL intensity at 0 K, k_B is Boltzmann constant, and E_b is EBE [44,46]. The EBE can be computed by the fitted curves (Fig. 6a-f). According to " $EDE = e^{-E_b/(k_B T)}$ " ($k_B T \approx 25$ meV at room temperature), the exciton dissociation efficiency (EDE) is calculated as 38.8 %, 39.4 %, 39.9 %, 41.1 %, 40.2 % and 39.7 % for CN, CCN-2, CCN-4, CCN-6, CCN-8 and CCN-12, respectively. Interestingly, the optimized in-plane crystallinity did not significantly reduce EBE or improve EDE, only decreasing EBE by 1.5 meV and increasing EDE by 2.3 %, respectively.

Hall effect tester is used to measure the carrier type, resistivity, Hall coefficient, carrier mobility and carrier concentration of materials. The samples are pressed into thin sheets by the tablet press, and then tested using the van der Pauw method. As shown in Table 1, the shape factor (f) of all tests is close to 1, indicating the symmetrical distribution of

samples. Both CN and CCN exhibit negative Hall coefficients, corresponding to electrons being major carriers and n -type semiconductors [47]. In addition, defects are one of the most important factors affecting carrier mobility. Defects can cause carrier scattering and trapping in the semiconductor, greatly reducing carrier mobility. Increasing in-plane crystallinity can reduce defects, hydrogen bonds and grain boundaries, thereby improving carrier mobility. The conductivity depends on the carrier concentration and carrier mobility. The carriers of CN and CCN originate from the thermal excitation at room temperature, and their concentrations have not increased significantly. On the contrary, due to the 3.7 times increase in carrier mobility, the conductivity is improved by 3.8 times (CN vs. CCN-6). In short, the conductivity and carrier mobility of the samples are consistent with the changes in in-plane crystallinity.

3.5. Analysis of the mechanism of enhancing photocatalytic activity

The optimized in-plane crystallinity does not significantly promote the EDE, but improves the conductivity and carrier mobility, which may be responsible for the increased photocatalytic activity. The specific surface area has a significant impact on photocatalytic activity, therefore the H_2 production rates of specific surface areas are normalized (Table S4). Taking ten kinds of CCN with different in-plane crystallinity as examples, we replotted the scatter diagram with the XRD diffraction intensity of in-plane (100) as the x-axis and normalized H_2 production rates of specific surface areas as the y-axis. As shown in Fig. 7a, these scattered points are distributed in the region from the lower left corner to the upper right corner and can be well-fitted by a linear function, indicating a positive correlation between in-plane crystallinity and photocatalytic activity.

Fig. 7b summarizes the C/N molar ratio, normalized H_2 production rates of specific surface areas, carrier mobility, conductivity and EDE in CN and CCN- x ($x = 2, 4, 6, 8, 12$) samples. The C/N ratio can reflect the degree of polymerization. With the further polymerization of free amino

Table 1

The measured resistivity, Hall coefficient, carrier concentration and carrier mobility using a van der Pauw Hall measurement system.

	Resistivity ($\Omega\text{-cm}$)	Hall coefficient (cm^3/C)	Carrier concentration ($1/\text{cm}^3$)	Carrier mobility ($\text{cm}^2/(\text{V}\cdot\text{s})$)	f-factor
CN	12400	-2470	4.18×10^{15}	0.128	0.9997
CCN-2	7230	-2820	4.40×10^{15}	0.238	0.9961
CCN-4	5220	-2310	4.70×10^{15}	0.369	0.9973
CCN-6	2540	-2670	5.34×10^{15}	0.604	0.9917
CCN-8	3780	-2720	5.00×10^{15}	0.513	0.9914
CCN-12	4210	-2950	4.85×10^{15}	0.440	0.9999

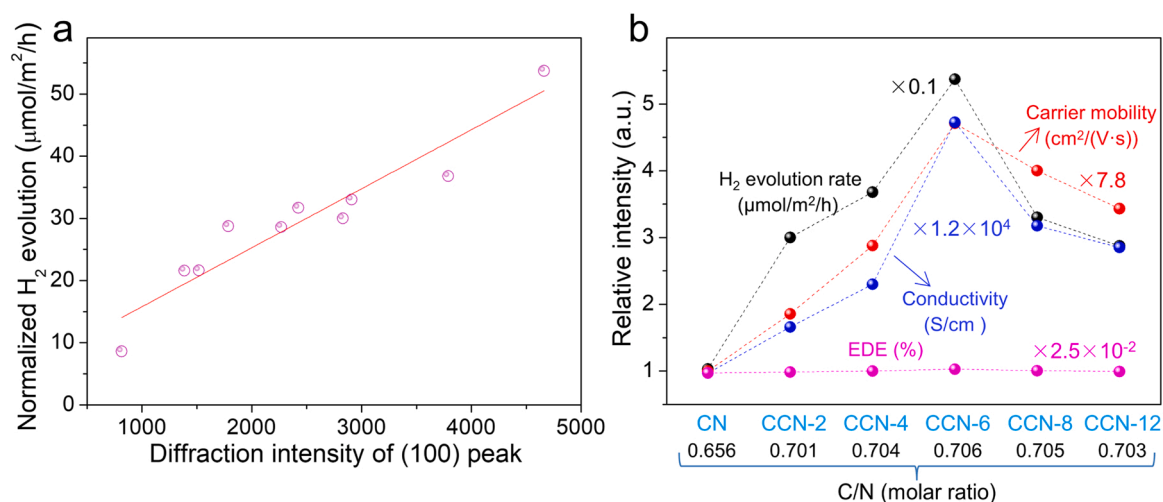


Fig. 7. Integrated normalized H_2 production rates of specific surface areas as a function of XRD diffraction intensity of in-plane (100) (a). The C/N molar ratio, normalized H_2 production rates, carrier mobility, conductivity and EDE in CN and CCN- x ($x = 2, 4, 6, 8, 12$) samples (b).

groups in the process of CN crystallization to form CCN, the C/N ratio increases from 0.656 to the theoretical value of 0.706. The increased degree of polymerization makes the in-plane highly-crystalline, thus accelerating the carrier migration and improving the conductivity. In order to better demonstrate the changing trend, we normalized the normalized H_2 production rates of specific surface areas, carrier mobility, conductivity and EDE of the CN sample to a position close to 1. As can be seen from Fig. 7b, the changes of EBE and EDE values are minor. The EDE is only increased by 2.3 % (CCN-6 vs. CN), which can

rule out the photocatalytic activity promoted by the exciton dissociation. The accelerated photocatalytic activity is more attributable to the improvement of polymerization degree, in-plane crystallinity, conductivity and carrier mobility than to the slight change of EDE.

The transport and separation behaviors of carriers were investigated by combining photoelectrochemical characterization, including steady-state photoluminescence (PL), time-resolved photoluminescence (TRPL), linear sweep voltammetry (LSV) and surface photovoltage spectroscopy (SPS). Compared with CN, CCN exhibits significantly

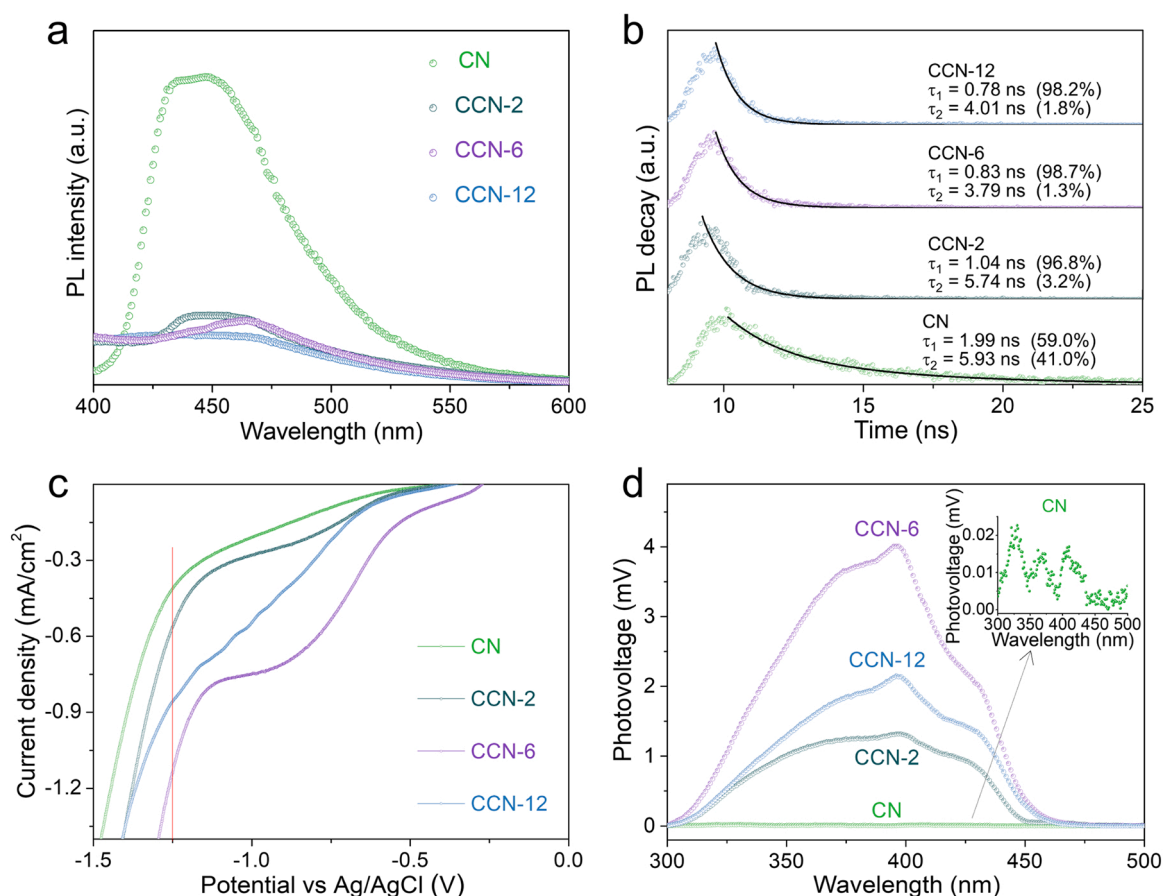


Fig. 8. The steady-state PL (a), TRPL (b), LSV (c) and SPS (d) of CN and CCN- x ($x = 2, 6, 12$) samples.

quenched interband fluorescence emission due to the enhanced in-plane crystallinity and accelerated carrier transport (Fig. 8a). In Fig. 8b, the TRPL can be well fitted as double exponential functions, which corresponds to the faster decay in the bulk (τ_1) and the slower decay in trap states (τ_2) [48,49]. The relative weight value of the defect recombination process drastically decreases from 41.0 % of CN to 3.2 % of CCN-2, 1.3 % of CCN-6 % and 1.8 % of CCN-12, because of fewer structural defects caused by the increased polymerization degree and in-plane crystallinity.

The transport behavior of the carrier is further analyzed by LSV measurements. As shown in Fig. 8c, the onset potentials of CN and CCN are located at -1.2 to 1.4 V (vs. Ag/AgCl). With the increase of potential, the current density related to the reduction capacitive behavior increases sharply, which is attributed to the H_2 evolution reaction [50]. In LSV test, the higher current density reflects the excellent charge transport ability to some extent [51–54]. At the same potential, such as 1.25 V, the relation of current density is $CCN-6 > CCN-12 > CCN-2 > CN$, consistent with the trends of conductivity, carrier mobility and photocatalytic activity. SPS is an effective means to investigate the behavior of photogenerated carriers at micro and nano scales, which can directly reflect the separation direction and efficiency (Fig. 8d) [55]. Both CN and CCN exhibit the positive surface photovoltage (SPV) signals of typical n -type semiconductors. In addition, the SPV signal of CCN is significantly higher than that of CN, and CCN-6 presents the highest SPV signal, which is due to the enhanced in-plane crystallinity that promotes the carrier migration and separation.

Transient absorption (TA) spectroscopy is a common ultrafast laser pump-probe technology, which is a powerful tool to investigate the relaxation dynamics of photogenerated carriers [56,57]. Both CN and CCN-6 are excited from the ground-state to the excited-state by 330 nm pump light. At different probe delays, the continuous signals of ground-state bleaching and excited-state absorption were observed between 450 and 800 nm (Fig. 9a,b,d,e). With the extension of probe

delays, the TA intensity decreases, indicating that the excited-state carriers decrease. In addition, the positive TA signal of CCN-6 sample is obviously stronger than that of CN, which corresponds to the generation and separation of more active carriers due to the improved conductivity and carrier mobility.

The kinetic traces were fitted at approximately 670 nm, the maximum absorption of TA spectra, to elucidate the relaxation dynamics of excited-state carriers (Fig. 9c,f). The ultrafast carrier relaxation dynamics of CN and CCN-6 are well-fitted as ternary exponential functions, which correspond to three different depths of electron trapped-states [58]. The shorter life components (τ_1 and τ_2) can be attributed to the deeper electron trapped-states, while the longer life (τ_3) is referred to as the shallower traps. Generally speaking, the long-lived shallow-trapped electrons are more active in photocatalytic reaction than the short-lived deep-trapped electrons [58,59]. Due to the higher degree of polymerization and optimized in-plane crystallinity, CCN-6 exhibits fewer deep traps (54.3 % vs. 74.5 %) and more shallow traps (45.7 % vs. 25.5 %) than CN, thus achieving higher charge separation efficiency and photocatalytic activity. In addition, the high mobility and long life of carriers will result in longer migration distances, making it easier to achieve spatial separation. Simultaneously, long-lived carriers have more opportunities to interact with surface-adsorbed substances, which is advantageous to photocatalysis.

4. Conclusions

In conclusion, ten kinds of CCN with different in-plane crystallinity were constructed by adjusting the types of molten-salts or solid-salt, proportions of molten-salts and holding times. The relationship between exciton dissociation, charge separation behavior and photocatalytic activity was well revealed. The conductivity and carrier mobility of the samples are consistent with the changes in in-plane crystallinity. Besides, the optimized in-plane crystallinity did not significantly reduce EBE or improve EDE, only decreasing by 1.5 meV

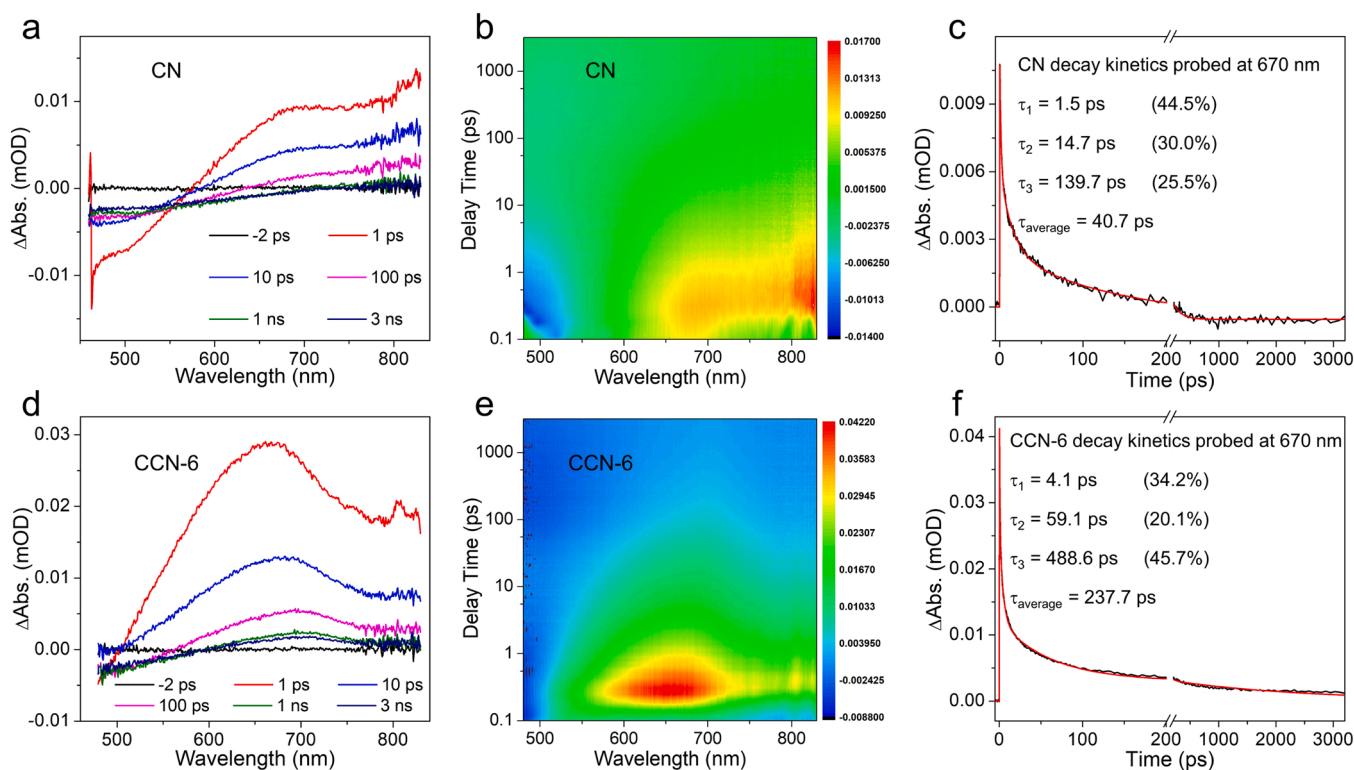


Fig. 9. Representative TA spectra at different probe delays (a,d) and time-wavelength-dependent TA color maps (b,e) (pump at 330 nm). TA decay kinetics probed at 670 nm (c,f).

and increasing by 2.3 %, respectively. On the contrary, the photocatalytic performance is more dependent on the degree of polymerization, carrier mobility and conductivity. Therefore, the accelerated photocatalytic activity is more attributable to the improvement of polymerization degree, in-plane crystallinity, conductivity and carrier mobility than the slight change of EDE.

CRedit authorship contribution statement

Guoqiang Zhang: Conceptualization, Methodology, Data curation, Software, Investigation, Writing – Original Draft, Funding acquisition. **Yangsens Xu:** Visualization, Writing - Review & Editing. **Jinyu Zhu :** Investigation. **Yongliang Li:** Supervision, Software. **Chuanxin He:** Supervision, Software. **Xiangzhong Ren:** Supervision, Software. **Peixin Zhang:** Supervision, Software, Funding acquisition. **Hongwei Mi:** Conceptualization, Supervision, Project administration, Writing - Review & Editing, Funding acquisition. All authors contributed to manuscript revision, read and approved the submitted version.

Declaration of Competing Interest

The authors declare that they have no known competing financial interests or personal relationships that could have appeared to influence the work reported in this paper.

Data Availability

Data will be made available on request.

Acknowledgments

This work was jointly supported by the National Science Foundation of China (22102103), Shenzhen Science and Technology Program (JCYJ20220531102617040) and Talent introduction project of Great Bay University (YJKY230013).

Appendix A. Supporting information

Supplementary data associated with this article can be found in the online version at [doi:10.1016/j.apcatb.2023.123049](https://doi.org/10.1016/j.apcatb.2023.123049).

References

- [1] A.J. Heeger, Semiconducting polymers: the third generation, *Chem. Soc. Rev.* 39 (2010) 2354–2371.
- [2] S. Brazovskii, N. Kirova, Physical theory of excitons in conducting polymers, *Chem. Soc. Rev.* 39 (2010) 2453–2465.
- [3] G. Zhang, Y. Xu, G. Liu, Y. Li, C. He, X. Ren, P. Zhang, H. Mi, Pyrimidine donor induced built-in electric field between melon chains in crystalline carbon nitride to facilitate excitons dissociation, *Chin. Chem. Lett.* 34 (2023), 107383.
- [4] G. Zhang, Y. Xu, D. Yan, C. He, Y. Li, X. Ren, P. Zhang, H. Mi, Construction of K⁺ ion gradient in crystalline carbon nitride to accelerate exciton dissociation and charge separation for visible light H₂ production, *ACS Catal.* 11 (2021) 6995–7005.
- [5] T. Hisatomi, J. Kubota, K. Domen, Recent advances in semiconductors for photocatalytic and photoelectrochemical water splitting, *Chem. Soc. Rev.* 43 (2014) 7520–7535.
- [6] F.E. Osterloh, Inorganic nanostructures for photoelectrochemical and photocatalytic water splitting, *Chem. Soc. Rev.* 42 (2013) 2294–2320.
- [7] H. Wang, S. Jiang, S. Chen, X. Zhang, W. Shao, X. Sun, Z. Zhao, Q. Zhang, Y. Luo, Y. Xie, Insights into the excitonic processes in polymeric photocatalysts, *Chem. Sci.* 8 (2017) 4087–4092.
- [8] J. Gorenflot, A. Paulke, F. Piersimoni, J. Wolf, Z. Kan, F. Cruciani, A.E. Labban, D. Neher, P.M. Beaujuge, F. Laquai, From recombination dynamics to device performance: quantifying the efficiency of exciton dissociation, charge separation, and extraction in bulk heterojunction solar cells with fluorine-substituted polymer donors, *Adv. Energy Mater.* 8 (2018), 1701678.
- [9] H. Tamura, I. Burghardt, Ultrafast charge separation in organic photovoltaics enhanced by charge delocalization and vibrationally hot exciton dissociation, *J. Am. Chem. Soc.* 135 (2013) 16364–16367.
- [10] J. Yuan, Y. Tang, X. Yi, C. Liu, C. Li, Y. Zeng, S. Luo, Crystallization, cyanamide defect and ion induction of carbon nitride: exciton polarization dissociation, charge transfer and surface electron density for enhanced hydrogen evolution, *Appl. Catal. B-Environ.* 251 (2019) 206–212.
- [11] F. Guo, B. Hu, C. Yang, J. Zhang, Y. Hou, X. Wang, On-surface polymerization of in-plane highly ordered carbon nitride nanosheets toward photocatalytic mineralization of mercaptan gas, *Adv. Mater.* 33 (2021), 2101466.
- [12] Z. Zhao, Z. Shu, J. Zhou, T. Li, F. Yan, W. Wang, L. Xu, L. Shi, Z. Liao, One-step fabrication of crystalline carbon nitride with tunable in-plane/interlayer crystallinity for enhanced photocatalytic hydrogen evolution, *J. Alloy. Compd.* 164828 (2022) 910.
- [13] G. Zhang, J. Zhu, Y. Xu, C. Yang, C. He, P. Zhang, Y. Li, X. Ren, H. Mi, In-plane charge transport dominates the overall charge separation and photocatalytic activity in crystalline carbon nitride, *ACS Catal.* 12 (2022) 4648–4658.
- [14] J. Woo Choi, H.C. Woo, X. Huang, W.-G. Jung, B.-J. Kim, S.-W. Jeon, S.-Y. Yim, J.-S. Lee, C.-L. Lee, Organic-inorganic hybrid perovskite quantum dots with high PLQY and enhanced carrier mobility through crystallinity control by solvent engineering and solid-state ligand exchange, *Nanoscale* 10 (2018) 13356–13367.
- [15] D.T. Scholes, P.Y. Yee, G.R. McKeown, S. Li, H. Kang, J.R. Lindemuth, X. Xia, S. C. King, D.S. Seferos, S.H. Tolbert, B.J. Schwartz, Designing conjugated polymers for molecular doping: the roles of crystallinity, swelling, and conductivity in sequentially-doped selenophene-based copolymers, *Chem. Mater.* 31 (2019) 73–82.
- [16] T.-N. Ye, M. Xu, W. Fu, Y.-Y. Cai, X. Wei, K.-X. Wang, Y.-N. Zhao, X.-H. Li, J.-S. Chen, The crystallinity effect of mesocrystalline BaZrO₃ hollow nanospheres on charge separation for photocatalysis, *Chem. Commun.* 50 (2014) 3021–3023.
- [17] F.K. Kessler, Y. Zheng, D. Schwarz, C. Merschjann, W. Schnick, X. Wang, M. J. Bojdy, Functional carbon nitride materials-design strategies for electrochemical devices, *Nat. Rev. Mater.* 2 (2017) 17030.
- [18] T. Botari, W.P. Huhn, V.W.-h Lau, B.V. Lotsch, V. Blum, Thermodynamic equilibria in carbon nitride photocatalyst materials and conditions for the existence of graphitic carbon nitride g-C₃N₄, *Chem. Mater.* 29 (2017) 4445–4453.
- [19] H. Schlöglberg, J. Kröger, G. Savasci, M.W. Terban, S. Bette, I. Moudrakovski, V. Duppel, F. Podjaski, R. Siegel, J. Senker, R.E. Dinnebier, C. Ochsenfeld, B. V. Lotsch, Structural insights into poly(heptazine imides): a light-storing carbon nitride material for dark photocatalysis, *Chem. Mater.* 31 (2019) 7478–7486.
- [20] G. Zhang, Y. Xu, M. Rauf, J. Zhu, Y. Li, C. He, X. Ren, P. Zhang, H. Mi, Breaking the limitation of elevated coulomb interaction in crystalline carbon nitride for visible and near-infrared light photoactivity, *Adv. Sci.* 9 (2022), 2201677.
- [21] Y. Xu, C. Qiu, X. Fan, Y. Xiao, G. Zhang, K. Yu, H. Ju, X. Ling, Y. Zhu, C. Su, K⁺-induced crystallization of polymeric carbon nitride to boost its photocatalytic activity for H₂ evolution and hydrogenation of alkenes, *Appl. Catal. B-Environ.* 268 (2020), 118457.
- [22] Y. Xu, X. He, H. Zhong, D.J. Singh, L. Zhang, R. Wang, Solid salt confinement effect: an effective strategy to fabricate high crystalline polymer carbon nitride for enhanced photocatalytic hydrogen evolution, *Appl. Catal. B-Environ.* 246 (2019) 349–355.
- [23] G. Zhang, G. Li, Z.-A. Lan, L. Lin, A. Savateev, T. Heil, S. Zafeirotas, X. Wang, M. Antonietti, Optimizing optical absorption, exciton dissociation, and charge transfer of a polymeric carbon nitride with ultrahigh solar hydrogen production activity, *Angew. Chem. Int. Ed.* 56 (2017) 13445–13449.
- [24] H. Ou, L. Lin, Y. Zheng, P. Yang, Y. Fang, X. Wang, Tri-s-triazine-based crystalline carbon nitride nanosheets for an improved hydrogen evolution, *Adv. Mater.* 29 (2017), 1700008.
- [25] L. Lin, H. Ou, Y. Zhang, X. Wang, Tri-s-triazine-based crystalline graphitic carbon nitrides for highly efficient hydrogen evolution photocatalysis, *ACS Catal.* 6 (2016) 3921–3931.
- [26] Z. Chen, A. Savateev, S. Pronkin, V. Papaefthimiou, C. Wolff, M.G. Willinger, E. Willinger, D. Neher, M. Antonietti, D. Dontsova, “The Easier the Better” preparation of efficient photocatalysts-metastable poly(heptazine imide) salts, *Adv. Mater.* 29 (2017), 1700555.
- [27] Y. Kang, Y. Yang, L.-C. Yin, X. Kang, L. Wang, G. Liu, H.-M. Cheng, Selective breaking of hydrogen bonds of layered carbon nitride for visible light photocatalysis, *Adv. Mater.* 28 (2016) 6471–6477.
- [28] A. Savateev, S. Pronkin, M.G. Willinger, M. Antonietti, D. Dontsova, Towards organic zeolites and inclusion catalysts: heptazine imide salts can exchange metal cations in the solid state, *Chem. Asian J.* 12 (2017) 1517–1522.
- [29] A. Savateev, S. Pronkin, J.D. Epping, M.G. Willinger, C. Wolff, D. Neher, M. Antonietti, D. Dontsova, Potassium poly(heptazine imides) from aminotetrazoles: shifting band gaps of carbon nitride-like materials for more efficient solar hydrogen and oxygen evolution, *ChemCatChem* 9 (2017) 167–174.
- [30] J. Zhang, G. Zhang, X. Chen, S. Lin, L. Möhlmann, G. Dolega, G. Lipner, M. Antonietti, S. Blechert, X. Wang, Co-monomer control of carbon nitride semiconductors to optimize hydrogen evolution with visible light, *Angew. Chem. Int. Ed.* 51 (2012) 3183–3187.
- [31] V.W.-h Lau, I. Moudrakovski, T. Botari, S. Weinberger, M.B. Mesch, V. Duppel, J. Senker, V. Blum, B.V. Lotsch, Rational design of carbon nitride photocatalysts by identification of cyanamide defects as catalytically relevant sites, *Nat. Commun.* 7 (2016) 12165.
- [32] B.V. Lotsch, M. Döblinger, J. Sehnert, L. Seyfarth, J. Senker, O. Oeckler, W. Schnick, Unmasking melon by a complementary approach employing electron diffraction, solid-state nmr spectroscopy, and theoretical calculations-structural characterization of a carbon nitride polymer, *Chem. Eur. J.* 13 (2007) 4969–4980.
- [33] S.-H. Wang, J. Yue, W. Dong, T.-T. Zuo, J.-Y. Li, X. Liu, X.-D. Zhang, L. Liu, J.-L. Shi, Y.-X. Yin, Y.-G. Guo, Tuning wettability of molten lithium via a chemical strategy for lithium metal anodes, *Nat. Commun.* 10 (2019) 4930.
- [34] J. Stoch, M. Ladecka, An XPS study of the KCl surface oxidation in oxygen glow discharge, *Appl. Surf. Sci.* 31 (1988) 426–436.
- [35] S. Cao, J. Low, J. Yu, M. Jaroniec, Polymeric photocatalysts based on graphitic carbon nitride, *Adv. Mater.* 27 (2015) 2150–2176.

- [36] G. Zhang, J. Zhang, M. Zhang, X. Wang, Polycondensation of thiourea into carbon nitride semiconductors as visible light photocatalysts, *J. Mater. Chem.* 22 (2012) 8083–8091.
- [37] L. Lin, W. Ren, C. Wang, A.M. Asiri, J. Zhang, X. Wang, Crystalline carbon nitride semiconductors prepared at different temperatures for photocatalytic hydrogen production, *Appl. Catal. B-Environ.* 231 (2018) 234–241.
- [38] A. Thomas, A. Fischer, F. Goettmann, M. Antonietti, J.-O. Müller, R. Schlögl, J. M. Carlsson, Graphitic carbon nitride materials: variation of structure and morphology and their use as metal-free catalysts, *J. Mater. Chem.* 18 (2008) 4893–4908.
- [39] G. Zhang, Y. Xu, C. He, P. Zhang, H. Mi, Oxygen-doped crystalline carbon nitride with greatly extended visible-light-responsive range for photocatalytic H₂ generation, *Appl. Catal. B-Environ.* 283 (2021), 119636.
- [40] G. Zhang, Y. Xu, H. Mi, P. Zhang, H. Li, Y. Lu, Donor bandgap engineering without sacrificing the reduction ability of photogenerated electrons in crystalline carbon nitride, *ChemSusChem* 14 (2021) 4516–4524.
- [41] F. Podjaski, J. Kröger, B.V. Lotsch, Toward an aqueous solar battery: direct electrochemical storage of solar energy in carbon nitrides, *Adv. Mater.* 30 (2018), 1705477.
- [42] F. Podjaski, B.V. Lotsch, Optoelectronics meets optoionics: light storing carbon nitrides and beyond, *Adv. Energy Mater.* 11 (2021), 2003049.
- [43] C. Bie, L. Wang, J. Yu, Challenges for photocatalytic overall water splitting, *Chem* 8 (2022) 1567–1574.
- [44] L. Lin, Z. Lin, J. Zhang, X. Cai, W. Lin, Z. Yu, X. Wang, Molecular-level insights on the reactive facet of carbon nitride single crystals photocatalysing overall water splitting, *Nat. Catal.* 3 (2020) 649–655.
- [45] L. Lin, C. Wang, W. Ren, H. Ou, Y. Zhang, X. Wang, Photocatalytic overall water splitting by conjugated semiconductors with crystalline poly(triazine imide) frameworks, *Chem. Sci.* 8 (2017) 5506–5511.
- [46] X. Li, Y. Wu, S. Zhang, B. Cai, Y. Gu, J. Song, H. Zeng, CsPbX₃ quantum dots for lighting and displays: room-temperature synthesis, photoluminescence superiorities, underlying origins and white light-emitting diodes, *Adv. Funct. Mater.* 26 (2016) 2435–2445.
- [47] A. Samanta, D.P. Arovas, A. Auerbach, Hall coefficient of semimetals, *Phys. Rev. Lett.* 126 (2021), 076603.
- [48] R. Brüninghoff, K. Wenderich, J.P. Korterik, B.T. Mei, G. Mul, A. Huijser, Time-dependent photoluminescence of nanostructured anatase TiO₂ and the role of bulk and surface processes, *J. Phys. Chem. C* 123 (2019) 26653–26661.
- [49] J. Kröger, A. Jiménez-Solano, G. Savasci, V. Wh Lau, V. Duppel, I. Moudrakovski, K. Küster, T. Scholz, A. Gouder, M.-L. Schreiber, F. Podjaski, C. Ochsenfeld, B. V. Lotsch, Morphology control in 2D carbon nitrides: impact of particle size on optoelectronic properties and photocatalysis, *Adv. Funct. Mater.* 31 (2021), 2102468.
- [50] Z. Zhang, L. Lu, Z. Lv, Y. Chen, H. Jin, S. Hou, L. Qiu, L. Duan, J. Liu, K. Dai, Porous carbon nitride with defect mediated interfacial oxidation for improving visible light photocatalytic hydrogen evolution, *Appl. Catal. B-Environ.* 232 (2018) 384–390.
- [51] W. Li, F. Wang, X. Liu, Y. Dang, J. Li, T. Ma, C. Wang, Promoting body carriers migration of CdS nanocatalyst by N-doping for improved hydrogen production under simulated sunlight irradiation, *Appl. Catal. B-Environ.* 313 (2022), 121470.
- [52] W. Li, Y. Dang, T. Ma, J. Li, G. Liao, F. Gao, W. Duan, X. Wang, C. Wang, Synergistic electric metal (Ni SAs)-semiconductor (CdS NPs) interaction for improved H₂O-to-H₂ conversion performance under simulated sunlight, *Sol. RRL* 7 (2023), 2300110.
- [53] W. Li, F. Wang, X. Chu, Y. Dang, X. Liu, T. Ma, J. Li, C. Wang, 3D porous BN/rGO skeleton embedded by MoS₂ nanostructures for simulated-solar-light induced hydrogen production, *Chem. Eng. J.* 435 (2022), 132441.
- [54] W. Li, X. Wang, Q. Ma, F. Wang, X. Chu, X. Wang, C. Wang, CdS@h-BN heterointerface construction on reduced graphene oxide nanosheets for hydrogen production, *Appl. Catal. B-Environ.* 284 (2021), 119688.
- [55] L. Kronik, Y.J.S. Shapira, I. Analysis, Surface photovoltage spectroscopy of semiconductor structures: at the crossroads of physics, chemistry and electrical engineering, *Surf. Interface Anal.* 31 (2010) 954–965.
- [56] J. Ma, T.J. Miao, J. Tang, Charge carrier dynamics and reaction intermediates in heterogeneous photocatalysis by time-resolved spectroscopies, *Chem. Soc. Rev.* 51 (2022) 5777–5794.
- [57] Berera, Rudi, V. Grondelle, Rienk, Kennis, T.M.J.S.N. John, Ultrafast transient absorption spectroscopy: principles and application to photosynthetic systems, *Photosynth. Res.* 101 (2009) 105–118.
- [58] R. Godin, Y. Wang, M.A. Zwijsenburg, J. Tang, J.R. Durrant, Time-resolved spectroscopic investigation of charge trapping in carbon nitrides photocatalysts for hydrogen generation, *J. Am. Chem. Soc.* 139 (2017) 5216–5224.
- [59] J.J. Walsh, C. Jiang, J. Tang, A.J. Cowan, Photochemical CO₂ reduction using structurally controlled g-C₃N₄, *Phys. Chem. Chem. Phys.* 18 (2016) 24825–24829.